



Label-free isolation of circulating tumor cells using negative lateral dielectrophoresis-assisted inertial microfluidics

Aliasghar Mohammadi¹ · Morteza Safari¹ · Mehdi Rahmanian²

Received: 29 March 2023 / Accepted: 6 July 2023 / Published online: 20 July 2023

© The Author(s), under exclusive licence to Springer-Verlag GmbH Germany, part of Springer Nature 2023, corrected publication 2023

Abstract

A dielectrophoresis (DEP)-assisted inertial microfluidics method is introduced in this study for the isolation of circulating tumor cells (CTCs) from diluted blood samples. The method is based on the negative DEP, provided with the laterally allocated microelectrodes as well as the proper selection of the applied electric field frequency and voltage to suppress the limited purity arising from the overlapped sizes of CTCs and white blood cells. The dynamics of polystyrene microparticles (with the sizes of 5 and 15 μm) were first investigated numerically and experimentally within the DEP-assisted inertial microfluidic device. While the dynamics of the larger microparticles were governed by the inertial and DEP forces, those of the smaller microparticles were subject to the Dean drag force. In the absence of the DEP force, the larger microparticles migrate to two stable equilibrium positions corresponding to the upper and lower walls for the microchannel cross section. In the presence of the DEP force, however, the equilibrium position corresponding to the lower wall is considerably displaced, while the top wall-associated equilibrium position remains almost intact. Finally, it was found that the proposed method outperformed the corresponding solely inertial method in terms of purity in the isolation of CTCs from diluted blood samples. For instance, at a hematocrit of 1%, the purity of isolated MDA-MB-231 cells spiked in diluted blood samples was 85.3% by the use of the solely inertial microfluidic device, while viable CTCs were captured by the DEP-assisted inertial microfluidic device with a purity of 94.1% at the total flow rate and applied voltage of, respectively, 650 $\mu\text{L min}^{-1}$ and 50 V.

1 Introduction

Despite the increasing clinical advances in cancer diagnosis and treatment, this disease has remained one of the deadliest diseases in the world (Siegal et al. 2014; Sleeboom et al. 2018). The high mortality rate of cancer arises from its aggressive spread throughout the body by a phenomenon known as metastasis (Fetah et al. 2019). Metastasis is responsible for more than 90% of cancer mortality. As a matter of fact, metastasis is the most significant barrier in our combat against cancer; such that cancer mortality does not decrease unless using a reliable biomarker to diagnose

metastasis at the early stages (Zhu et al. 2020; Hao et al. 2018).

During metastasis, circulating tumor cells (CTCs) are released from the primary tumor and transferred to distant organs via circulation (Zhu et al. 2020; Hao et al. 2018). Therefore, CTCs play a pivotal role in the development of secondary tumors (Zhu et al. 2020; Guan 2015). The significance of metastasis is more clarified considering that a 1 g tumor releases more than two million CTCs per day (Habli et al. 2020). However, CTCs have a limited half-life and many of them fail to survive the physical tensions in the bloodstream (Mishra et al. 2020). Nevertheless, few detached survived CTCs can spread cancer by developing tumors in other organs (Liu et al. 2021). Apart from the formation of secondary tumors, the lack of a unique prescription for all patients due to the heterogeneity of tumor cells is another challenge, which increases cancer mortality. In this regard, personalized therapy can lead to a shorter and more effective treatment period (Esmailsabzali et al. 2013).

The current approaches for cancer diagnosis hinge upon invasive procedures, such as tissue and bone biopsy. In this context, enumeration and isolation of CTCs can be

✉ Aliasghar Mohammadi
amohammadi@sharif.edu

¹ Department of Chemical and Petroleum Engineering, Sharif University of Technology, Tehran, Iran

² Biomaterials and Tissue Engineering Research Group, Interdisciplinary Technologies Department, Breast Cancer Research Center, Motamed Cancer Institute, ACECR, Tehran, Iran

an alternative strategy for early diagnosis of cancer in a less-invasive manner. Moreover, this approach provides a real-time assessment of the patient's condition as it simply demands a blood sample or other body fluids (Goh and Lim 2018). In other words, the number of CTCs in the blood could be an indicator of the tumor response to a specific therapy (Warkiani et al. 2014). Furthermore, capturing viable CTCs provides the opportunity for *in vitro* studies to develop anti-cancer drugs (Yang et al. 2019; Sharma et al. 2018). However, the isolation of CTCs is challenging due to their low concentration and size, which overlaps those of white blood cells (WBCs) (Lim et al. 2019).

Conventional techniques for the isolation of CTCs include density gradient centrifugation, flow cytometry, and fluorescence-activated as well as magnetic-activated cell sorting. Even though such techniques are well established, they require bulky and expensive equipment as well as detailed protocols. On the other hand, microfluidic-based techniques provide the opportunity to regulate and process a small amount of sample within a short time at a lower cell separation cost. As such, microfluidics has increasingly come into focus for cell separation and manipulation purposes (Fallahi et al. 2019; Gertler et al. 2003; Zheng et al. 2007).

In general, microfluidic-based cell separation techniques include two groups of passive and active. While passive techniques rely on differences among some intrinsic properties of cells, such as their size, shape, and deformability (Pødenphant et al. 2015; Au et al. 2017), active techniques use external forces for separating cells upon differences in their dielectric properties, magnetic susceptibility, compressibility, or refractive index (Rahmani et al. 2018; Wang et al. 2009; Zhao et al. 2016; Undvall Anand et al. 2021; Buican et al. 1987).

Among the passive techniques, inertial-based methods have been in focus for the separation of cancer cells in the last two decades (see section S1.1 of the supporting information for a brief introduction on the inertial migration in microchannels) (Xiang and Ni 2022; Hou et al. 2013; Carlo 2009; Mach et al. 2011). In this context, various microchannels with diverse geometries were reported to improve the isolation of CTCs (Warkiani et al. 2014; Hou et al. 2013; Erdem et al. 2020; Zhang et al. 2014; Lee et al. 2013; Guan et al. 2013; Ghadami et al. 2017). However, the contamination of isolated CTCs with WBCs is inevitable in size-based inertial microfluidics separations, due to the overlapped sizes of CTCs and WBCs (see section S1.2 of the supporting information for a brief introduction to blood cells) (Khan and Chen 2022). Moreover, the separation of cells is not easily regulated in inertial-based methods once the microfluidic device geometry is fixed.

Keeping this in mind, active methods can be utilized for separating same-sized cells, where the separation performance can be modulated by tuning externally controllable

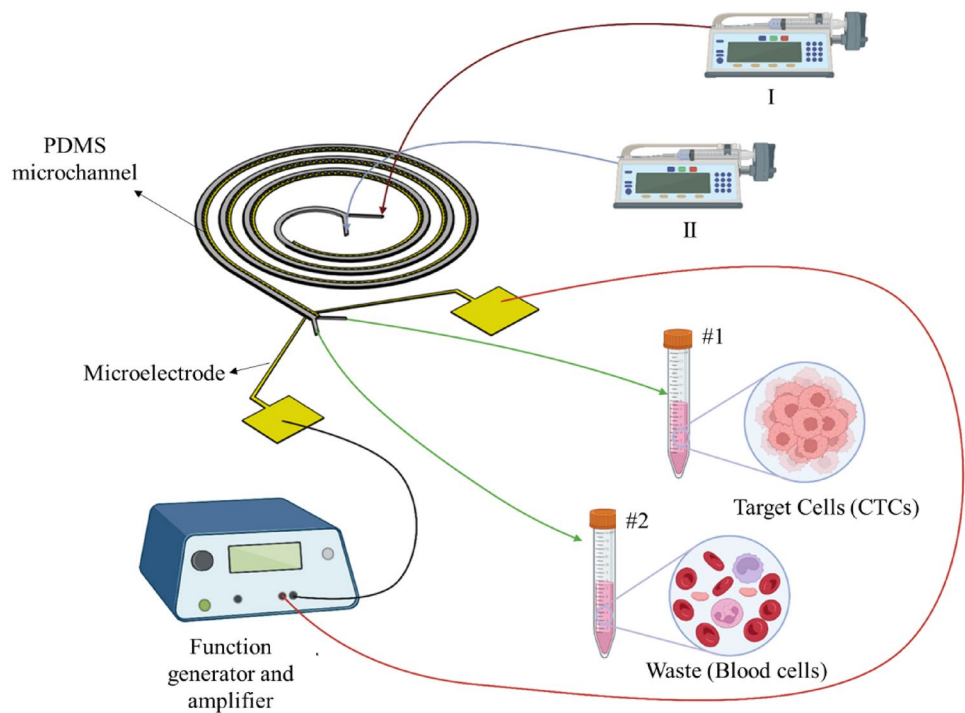
parameters. Nevertheless, active methods are a proper choice for cell separation at limited throughput (Cha et al. 2021).

In this regard, hybrid platforms have been developed for cell separation. A combination of the high precision active methods with the high-throughput inertial-based methods can result in a robust cell separation platform. Among the previously reported hybrid systems (Ozkumur et al. 2013; Huang and Xiang 2021; Kim et al. 2022; Sorour Amini and Mohammadi 2023), synergizing inertial-based methods with dielectrophoresis (DEP) appears a proper solution. In this venue, the studies reported as the inertial-DEP combination was a hybrid inertial-DEP platform (Zhang et al. 2018) in which the DEP was introduced through full coupling with a serpentine microchannel. A sheath fluid was also used to eliminate the upper inertial equilibrium positions. The DEP force was competing with the inertial lift force along the vertical direction, levitating particles in the vertical direction. Subsequently, differential focusing positions of particles were attained along the lateral direction. The inertial-DEP platform, however, demanded a careful selection of operational parameters to modulate the equilibrium positions. For instance, the positions were laterally differentiated at specific voltages; otherwise, no lateral differential focusing was observed. As such, there is still a lack of an inertial-DEP platform to easily control the equilibrium positions along the lateral direction.

In this study, a spiral microchannel was coupled with laterally allocated microelectrodes to form a, so-called, spiral-DEP microfluidic device (Fig. 1). The developed platform had many advantages over the current microfluidics particle manipulation methods. The proposed method is based on negative dielectrophoresis such that particles are not exposed to the strong electric fields near the microelectrodes. This is especially important for bioparticles, where prolonged exposure to strong electric fields leads to cell damage. In this context, the developed platform was used to isolate CTCs from blood. The designed microelectrodes were responsible for the deflection of the non-target cells toward the outer wall based on a negative DEP force as well as the crossover frequencies of different bioparticles. All types of non-target cells were removed, irrespective of their size overlap with target cells, by taking advantage of the selective inertial focusing for the inertial section and negative DEP for the dielectrophoresis section. Thus, WBC contamination was avoided in a label-free approach.

The remainder of this study is laid out as follows—a brief introduction on the dielectrophoresis is presented in Sect. 2. Section 3 outlines the design and simulation of the microfluidic device. Fabrication and sample preparation as well as operating procedures are discussed in Sects. 4 and 5, respectively. Section 6 is devoted to the results and discussion. Finally, a summary is given in Sect. 7.

Fig. 1 Schematic diagram of the experimental setup. Syringe pumps I and II were employed for the injection of the blood sample spiked with CTCs and sheath fluid, respectively. A generated and amplified electrical voltage was applied to the microelectrodes through copper wires



2 Theory of dielectrophoresis

When dielectric particles are exposed to a non-uniform electric field, the particles experience an external force, which is called the DEP force. For spherical particles, the DEP force is (Zhang et al. 2019)

$$F_{\text{DEP}} = \frac{\pi}{4} \epsilon_m d_p^3 \text{Re}[f_{\text{cm}}] \nabla |E|^2, \quad (1)$$

where ϵ_m is the permittivity of the medium, E shows the electric field vector, and $\text{Re}[f_{\text{cm}}]$ represents the real part of the Clausius–Mossotti factor. For spherical particles, the Clausius–Mossotti factor is (Zhang et al. 2019)

$$f_{\text{cm}} = \frac{\epsilon_p^* - \epsilon_m^*}{\epsilon_p^* + 2\epsilon_m^*}, \quad (2)$$

where ϵ_p^* and ϵ_m^* are the complex permittivity of the particles and medium, respectively, given by Zhang et al. (2019)

$$\epsilon^* = \epsilon - \frac{i\sigma}{\omega}, \quad (3)$$

with ϵ being the permittivity. σ denotes the electrical conductivity, and ω stands for the angular frequency of the electric field.

The real part of the Clausius–Mossotti factor ranges from -0.5 to 1 . When $\text{Re}[f_{\text{cm}}] > 0$, particles are pulled toward regions with higher electric field gradients as a result of positive DEP force. For $\text{Re}[f_{\text{cm}}] < 0$, negative DEP force pushes particles away from large electric field gradient

regions. Needless to say, particles do not experience DEP force when $\text{Re}[f_{\text{cm}}] = 0$.

3 Design and simulation of the microfluidic device

In this study, a spiral microchannel with three turns as well as two inlets and two outlets was employed. While the inner radius of the spiral microchannel was 6 mm , the distance between the turns was 1 mm . Moreover, the width of the microchannel cross section was $500 \mu\text{m}$ and the corresponding depth was $170 \mu\text{m}$. The inner and the outer inlets were employed for the injection of the sheath fluid and sample, respectively (Fig. 1). In the case of the biological sample, the sample was diluted CTC-spiked blood while the sheath fluid was phosphate-buffered saline (PBS). In addition, CTCs and blood cells were to come out of the microchannel through the inner and outer outlets, respectively. In other words, the CTCs and the blood cells were the target and non-target cells, respectively.

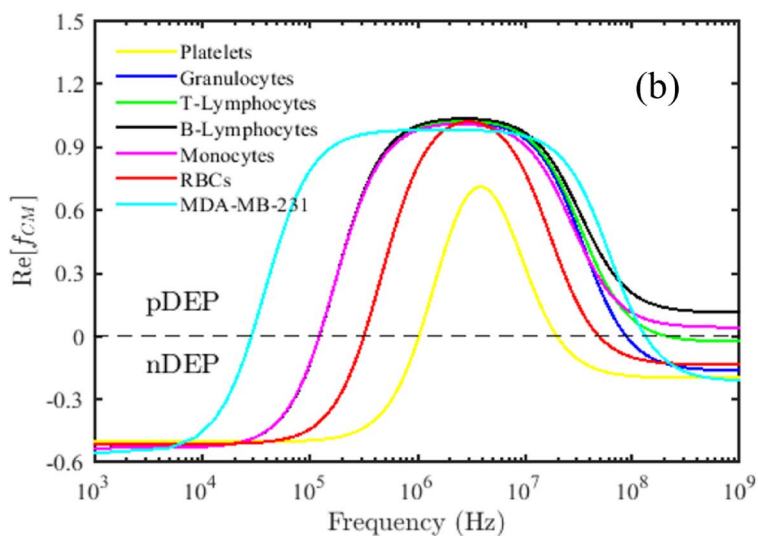
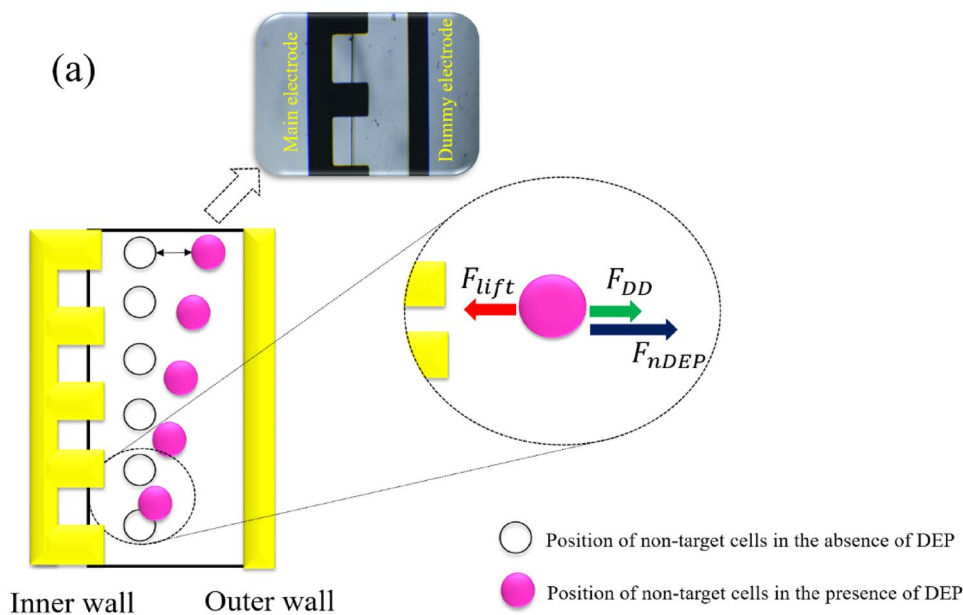
The tumor-derived breast cancer MDA-MB-231 cell line, as a typical circulating tumor cell, was used in this study to simulate the CTCs (see section S1.3 of the supporting information for a brief introduction to MDA-MB-231 cell line). Note also that the blood cells contain many types of cells: white blood cells (monocytes, lymphocytes, neutrophils, eosinophils, and basophils), red blood cells (RBCs—erythrocytes), and platelets.

Although many of the non-target cells are removed in the spiral microchannel using the Dean cycle phenomenon (see section S1.1 of the supporting information), such microfluidic devices fail to remove those non-target cells whose size overlaps the size of the target cells. Given the size distributions of the blood cells and MDA-MB-231 cell line (see sections S1.2 and S1.3 of the supporting information), the target cells have overlapped sizes with some many of the WBCs, which are called large WBCs in the remaining.

In the developed spiral microchannel, the CTCs and large WBCs focus close to the inner wall, reducing the purity of the isolated CTCs. To increase the purity of

the isolated CTCs, the DEP force was employed to push WBCs away from the inner wall. In this venue, the conventional practice to generate such negative DEP force involves embedding microelectrodes on one side of the microchannel. However, this approach was challenging due to geometrical restrictions. As such, an unprecedented microelectrode pattern (Figure S1) was designed to generate the negative DEP force to repel inertially focused large WBCs away from the inner wall. As depicted in Fig. 2a, the generated negative DEP force changes the equilibrium positions of the large WBCs toward the outer wall.

Fig. 2 Schematic top view of the microchannel and microelectrodes together with the trajectory of WBCs in the absence and presence of DEP generated by the microelectrodes (a). The real part of the Clausius–Mosotti factor, $Re[f_{CM}]$, for blood cells and CTCs as a function of frequency in PBS as a medium with the conductivity and relative permittivity of 0.01 S m^{-1} and 80, respectively (Aghaamoo et al. 2019). The single-shell approach was used to model the cells with the required properties given in Tables S2 and S3



We performed a three-dimensional simulation to analyze micro- and bioparticles dynamics in the spiral-DEP microfluidic device. For this purpose, all the blood cells were considered rigid spherical particles with diameters of 5, 15, and 15 μm to represent RBCs, large WBCs, and the CTCs, respectively. The considered physical characteristics and population of the cells in our simulations are listed in Table S2. Also, the particle tracing module was employed to address the dynamics of the cells within the microfluidic device through the Newton law of motion

$$\frac{d(m_p \mathbf{u}_p)}{dt} = \mathbf{F}_{\text{Drag}} + \mathbf{F}_{\text{Added Mass}} + \mathbf{F}_{\text{Lift}} + \mathbf{F}_{\text{DEP}}, \tag{4}$$

where m_p is the particle mass, \mathbf{u}_p denotes the particle velocity. \mathbf{F}_{Drag} , $\mathbf{F}_{\text{Added Mass}}$, \mathbf{F}_{Lift} , and \mathbf{F}_{DEP} also stand for the drag, added mass, resultant inertial lift, and DEP forces, respectively. Drag and added mass forces are

$$\mathbf{F}_{\text{Drag}} = 3\pi\mu d_p(\mathbf{u} - \mathbf{u}_p) \tag{5}$$

and

$$\mathbf{F}_{\text{Added Mass}} = (\pi/12)\rho d_p^3 \frac{d}{dt}(\mathbf{u} - \mathbf{u}_p), \tag{6}$$

where \mathbf{u} is the fluid velocity, which must be determined to calculate the drag and added mass forces.

The fluid velocity was determined by solving the equations of the mass- and momentum-conservation laws for the corresponding fluid within the spiral microchannel. For this purpose, the fluid was considered an incompressible Newtonian fluid. The momentum-conservation law of the fluid requires

$$\rho \left[\frac{\partial \mathbf{u}}{\partial t} + (\mathbf{u} \cdot \nabla) \mathbf{u} \right] = \mu \nabla^2 \mathbf{u} - \nabla p, \tag{7}$$

where p denotes the fluid pressure. As the fluid is incompressible, the mass-conservation law demands

$$\nabla \cdot \mathbf{u} = 0. \tag{8}$$

It must be noted that the blood is per se a shear-thinning fluid. But the blood is diluted with PBS in clinical cell separation applications as well as in our experiments. Therefore, the assumption of the blood as an incompressible Newtonian fluid is reasonable (Gijzen et al. 1999). Also, the physical properties of the fluid were set constant. The boundary conditions at the inlets involved fully developed velocities for the sample and sheath fluid. For the outlets, atmospheric pressure was assumed. Also, the no-slip boundary conditions were adopted for the fluid velocity at the microchannel walls.

Equations 7 and 8 were solved using the COMSOL Multiphysics software version 5.6, which is a finite element-based computational fluid dynamics software. In this venue, the laminar flow module was employed under

isothermal conditions at stationary mode. Moreover, the quadratic discretizing scheme was adopted for both velocity and pressure. The relative error in numerical calculations was considered 0.001. Furthermore, structured mesh elements were generated for the simulation with the optimum number of the elements being obtained using the mesh independency analysis. The details of the mesh independency analysis are presented in section S4 of the supporting information. Moreover, parallelized computations were performed for the simulations on 24-core high-performance computing clusters.

Returning to Eq. 4, the resultant inertial lift force must be also calculated to track the dynamics of the cells. Various approaches have been used to calculate the inertial lift forces; among which, explicit equations are an approximate one. Commercial softwares, such as the COMSOL Multiphysics software, employ an explicit equation to calculate the resultant inertial lift force as suggested by Ho and Leal. This approach, however, suffers from few restrictions, including finite Re numbers for the suspending medium. Also, such an equation cannot be employed in many-body practical situations (Ho and Leal 1974).

In this study, the Di Carlo algorithm was employed for calculating the resultant inertial lift force (Carlo et al. 2009). This algorithm was explained in detail in section S5 of the supporting information. The calculated inertial lift forces were mapped on the proposed spiral microchannel as a point force.

Finally, the DEP force must be calculated using Eq. 1 to ascertain the cell dynamics. For this purpose, the electrostatic potential distribution in the microchannel was determined by solving the Laplace equation ($\nabla \varphi^2 = 0$ with φ being the electrostatic potential) (Mohammadi 2015). To this end, the electric current physic module in the COMSOL Multiphysics software was employed. Then, the frequency-dependent approach was used to compute the electrostatic potential. Subsequently, the DEP force was calculated using Eq. 1.

It must be noted that DEP-based cell separation platforms rely on differences in the dielectric properties of the cells, where the electric field frequency has a modulating impact on the properties. Hence, a proper frequency was selected using a dielectrophoretic spectrum in which $\Re\{f_{cm}\}$ is plotted as a function of frequency for all cells. For plotting the spectrum, the single-shell model was adopted for calculating the dielectric properties of RBCs, WBCs, and CTCs in which the equivalent permittivity and conductivity of the cells were determined by

$$\epsilon_{eq}^* = \epsilon_{mem}^* \frac{\alpha^3 + 2\beta}{\alpha^3 - 2\beta} \tag{9}$$

with

$$\alpha = \frac{r}{r-d} \quad (10)$$

and

$$\beta = \frac{\epsilon_{\text{cyt}}^* - \epsilon_{\text{mem}}^*}{\epsilon_{\text{cyt}}^* + 2\epsilon_{\text{mem}}^*}. \quad (11)$$

Note that ϵ_{mem}^* is the shell permittivity. r and d respectively denote the radius of the corresponding cell and the shell thickness. ϵ_{cyt}^* represents the cytoplasm permittivity of the corresponding cell. Table S3 shows the single-shell model parameters for typical blood and cancer cells adopted in this study. In the developed microfluidic device, non-target cells should undergo negative DEP while the target cells experience negligible DEP. Therefore, as revealed by the plots in Fig. 2b, the frequency was set to 30 kHz.

After the determination of all forces contributing to the dynamics of cells in the developed microfluidic device, the particle tracing analysis was implemented to examine the cell dynamics in the spiral-DEP microfluidic device. For this purpose, Eq. 1 was solved using the particle tracing module in the COMSOL Multiphysics software in a time-dependent mode. To this end, all particles were abruptly introduced to the microfluidic device with zero initial velocity. Then, the particles went through the spiral microchannel with a velocity governed by Eq. 1 through coupling the laminar flow and particle tracing modules within the software.

The interparticle interactions were neglected in the numerical analysis. This assumption is guaranteed considering the concentration of cells in our experiments. While the volume fraction of cells in the studied samples was more than 1 vol.%, the employed sheath fluid was diluting the samples within the microfluidic device such that the resulting concentration fell below 0.2 vol.%. As such, ignoring interparticle interactions is warranted in our simulations (Sun et al. 2012).

4 Fabrication of the microfluidic device

The proposed microfluidic device comprised two parts: the microchannel and the microelectrodes. While the former was fabricated by standard soft-lithography procedure, the microelectrodes were prepared by conventional photolithography.

At the beginning, the pattern of the microchannel was designed using the AutoCAD 2000 software. A silicon wafer, as a substrate, was rinsed with, sequentially, acetone, isopropyl alcohol, as well as double-distilled water and, then, dried with a nitrogen stream. Afterward, hexamethyl disilazane was coated on the substrate using a spin coater (SC5, Samaneh Tajhiz) at 750 rpm for 60 s to improve the photoresist adhesion

to the wafer. The negative photoresist (SU8-2050, Microchem) was coated on the wafer to achieve 170 μm thickness. To this end, the photoresist was poured on the wafer surface. The spin coater angular velocity was increased to 750 rpm in 2.5 s, and was kept at the angular velocity for 57.5 s. Subsequently, the velocity was increased to 1400 rpm in 4.7 s, and was kept at the angular velocity for 55.3 s. Finally, the spin coater was stopped. The angular velocity of the spin coater was increased or decreased at a constant ramp of 300 rpm s^{-1} for all steps.

The resulting wafer was sequentially baked on a hot plate at 65 $^{\circ}\text{C}$ for 4 min and 95 $^{\circ}\text{C}$ for 19.5 min. After that, a negative photomask was placed on the baked wafer and, then, was exposed to the ultra-violet light (UV) for 60 s. The exposed substrate was sequentially baked at 65 $^{\circ}\text{C}$ for 1 min and 95 $^{\circ}\text{C}$ for 9.5 min. After the post-exposure bake, the substrate was immersed in a developing solution for 9.5 min. Finally, the substrate was baked at 150 $^{\circ}\text{C}$ for 2 min after visual inspection.

After preparation of the master mold (Figure S5a), 10 g polydimethylsiloxane (PDMS) was mixed with 1 g of its curing agent (Sylgard 184, Dow Corning). After degassing the resulting mixture, it was poured on the prepared mold and, then, cured in a vacuum oven at 80 $^{\circ}\text{C}$ and 0.4 mbar for 2 h. Finally, the PDMS layer was separated from the mold.

In the next step, the following instruction was implemented for fabricating the microelectrodes. First, a thin layer of gold and titanium (120 nm gold and 30 nm titanium) was deposited on a glass substrate ($60 \times 60 \times 1 \text{ mm}^3$) using the conventional sputtering (SP7 sputter, SATALAB). Then, a positive photoresist (S1813, Shipley) was coated on the resulting substrate and, subsequently, baked at 95 $^{\circ}\text{C}$ for 2 min. After cooling the substrate to room temperature, a photomask was placed on it and exposed to UV light for 80 s. Afterward, the resulting substrate was developed and, again, baked at 95 $^{\circ}\text{C}$ for 1 min. Finally, the extra gold and titanium were removed by wet etching, and the photoresist washed out with acetone (figure S5b).

Despite many DEP-based cell separation platforms employing plasma bonding, a clamp-type bonding was used in this study in which PDMS and glass were bonded by two poly(methyl methacrylate) sheets (see figure S5c). Without a doubt, each bonding method has its own merits. But our employed bonding method is temporary such that the microchannel and microelectrodes can be separated for cleaning. Another advantage of this bonding method is the suppressed fluid stress-induced PDMS microchannel deformation (Bazaz et al. 2022; Shrestha et al. 2023).

5 Sample preparation and operating procedures

In this study, the microfluidic device was tested with two distinct samples: polystyrene microparticles (non-biological sample) and diluted blood samples spiked with

MDA-MB-231 cell line (biological sample). The procedure of the sample preparation comprised two parts, which are explained in the following.

In the first part, polystyrene microparticles with an average diameter of 5 and 15 μm were suspended in deionized water with the conductivity and relative permittivity being, respectively, $2 \times 10^{-4} \text{ S m}^{-1}$ and 78.5 (Yafouz et al. 2014). The concentration of the polystyrene microparticles was adjusted to 0.1 vol.%. Then, Tween 20 (Sigma-Aldrich) at 0.5 wt.% was added to the suspension in order to prevent adhesion and aggregation of the microparticles. In addition, the resulting suspension was sonicated in an ultrasonic bath (Pars nahand, Parsonic 2600 s) for 30 min.

In the second part, the MDA-MB-231 cells were cultured in high-glucose Dulbecco's modified Eagle's medium (Gibco) in combination with 9 vol.% fetal bovine serum (BSA; Gibco) and 1 vol.% penicillin–streptomycin (Gibco). As part of the cultivation process, the cells were grown in T25 flasks at 37 °C in a humidified incubator with 5 vol.% CO_2 . When the cells reached 80–90% confluency, they were washed with $1 \times \text{PBS}$ and trypsinized with trypsin–ethylenediamine-tetra-acetic acid (EDTA). In addition, the CTCs were stained with 4',6-diamidino-2-phenylindole (DAPI; Beyotime Institute of Biotechnology, USA) to have a better visualization after separation from the blood cells. To this end, the cells were fixed with formaldehyde (4 vol.%) and, then, stained with DAPI.

The whole blood sample was obtained from a healthy donor for all experiments. EDTA solution (Sigma-Aldrich) was added to the blood sample (3.5 μL EDTA:1 mL blood) as an anticoagulant. Afterward, the anticoagulated blood sample was diluted with PBS containing 0.5% (wt./vol.) bovine serum albumin at different levels of hematocrit (1, 5, and 10 vol.%). Finally, MDA-MB-231 cells were added to the diluted blood samples, providing 2×10^4 CTCs mL^{-1} .

In this venue, it must be realized that handling diluted blood samples with limited hematocrit levels are not practical in clinical applications as large volumes should be processed, which is time-consuming and tedious. Without a doubt, higher throughput is required for practical applications to make the spiral-DEP microfluidic device a feasible solution for the isolation of CTCs. To address the limited capacity, several parallel microfluidic devices can be employed to achieve the required lab-scale capacity. This so-called number-up enables handling a large amount of diluted blood samples.

Two types of experiments were, however, performed with the spiral-DEP microfluidic device. In the earlier experiments, the physics of solely inertial as well as inertial-DEP microfluidics was examined by separating the polystyrene microparticles. In the latter experiments, the isolation of CTCs was addressed using the spiral-DEP microfluidic device with the diluted blood samples spiked with

the MDA-MB-231 cell line. The details of the operating procedures are described in section S8 of the supporting information.

In each experiment, the prepared sample was injected into the microfluidic device together with the sheath fluid. While deionized water was opted as the sheath fluid for the former experiments, the sheath fluid was PBS for the latter experiments. Moreover, the sample flow rate was $100 \mu\text{L min}^{-1}$ and the sheath fluid flow rate ranged from 150 to $750 \mu\text{L min}^{-1}$.

It must be realized that the aim of increasing the flow rate is to boost the inertial lift forces. For this purpose, the flow rate of either the sample or sheath fluid can be increased. Once the sheath fluid flow rate is constant, the concentration of the micro- and bioparticles becomes greater than 0.2 vol.% upon increasing the sample flow rate. In this situation, the interparticle interactions become considerable, producing significant effects on the dynamics of the particles within the microfluidic device. As such, the sample flow rate was kept constant and the sheath fluid flow rate was increased.

Additionally, all the micro- and bioparticles are to be focused close to the outer wall at the entrance region of the spiral-DEP microfluidic device with the aid of the sheath fluid. Once the sample flow rate increases and the sheath fluid flow rate is kept constant, the sheath fluid flow would not be strong enough to achieve the aimed focusing at the entrance region for the sample flow rates beyond the sheath fluid flow rate.

Meanwhile, three measures were used for the interpretation of the resulting data and assessing the microfluidic device performance:

$$\text{Efficiency} = \frac{\text{number of targeted particles/cells in the inner outlet}}{\text{number of targeted particles/cells in the inlet}}, \quad (12)$$

$$\text{Purity} = \frac{\text{number of targeted particles/cells in the inner outlet}}{\text{number of particles/cells in the inner outlet}}, \quad (13)$$

and

$$\text{Rejection ratio} = 1 - \frac{\text{number of blood cells in the inner outlet}}{\text{number of blood cells in the inlet}}. \quad (14)$$

Later, a trypan blue exclusion assay was performed in solely inertial and inertial-DEP platforms to measure the viability of the CTCs. It must be noted an unstained MDA-MB-231 cell line sample was also prepared for viability tests, apart from the stained MDA-MB-231 cell line. For this purpose, the CTCs were stained with a 0.4 vol.% trypan blue solution at room temperature. Then, the hemocytometer chamber was employed to count dead (blue-stained) and alive (unstained) cells (Sharma et al. 2018).

In addition, a flow cytometer (Attune NxT Flow Cytometer, Thermo Fisher Scientific) was used to assess the

reduction in the contamination of isolated CTCs with WBCs. For this purpose, the inner outlet from the spiral-DEP microfluidic device was stained by CD45 antibody (1:100) and, then, the CD45 expression on WBCs was examined in the absence and presence of the DEP through processing and analyzing the ascertained data from the flow cytometer using the FlowJo software version 7.

6 Results and discussion

The aim of this study is to improve the purity of the CTCs isolation from blood utilizing the synergistic effect of the inertial and dielectrophoresis phenomena. In this regard, the dynamics of different-sized polystyrene microparticles were numerically and experimentally investigated within the spiral microfluidic device. In the second part of this section, the dielectrophoretic force was applied to manipulate the lateral positions of the microparticles in the spiral-DEP microfluidic device. Finally, in the last part of this section, the isolation of the CTCs from blood was experimentally

investigated to examine the robustness of the spiral-DEP microfluidic device.

6.1 Dynamics of microparticles in the spiral microfluidic device

The dynamics of polystyrene microparticles, with the sizes of 5 and 15 μm , in the spiral microfluidic device were simulated at various flow rates. Figure 3 depicts the distance of the microparticles from the inner wall at the outlet of the spiral microfluidic device. The total flow rate considerably modulates the position of all the particles.

This observation is explained by considering the forces governing the dynamics of the microparticles. At the entrance region of the spiral microfluidic device, the particles were focused close to the outer wall with the aid of the sheath fluid. In such a situation, the particle motion is governed by the competition between the inertial lift force F_{lift} and the drag force exerted by the Dean vortices F_{Dean} . Due to the different scaling of these forces $|F_{\text{lift}}| \sim d_p^4$ and $|F_{\text{Dean}}| \sim d_p$, the microparticles undergo two different

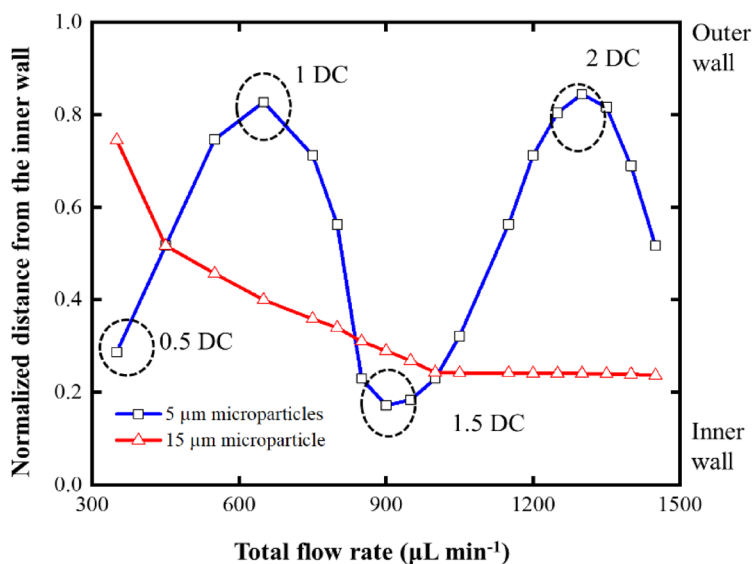
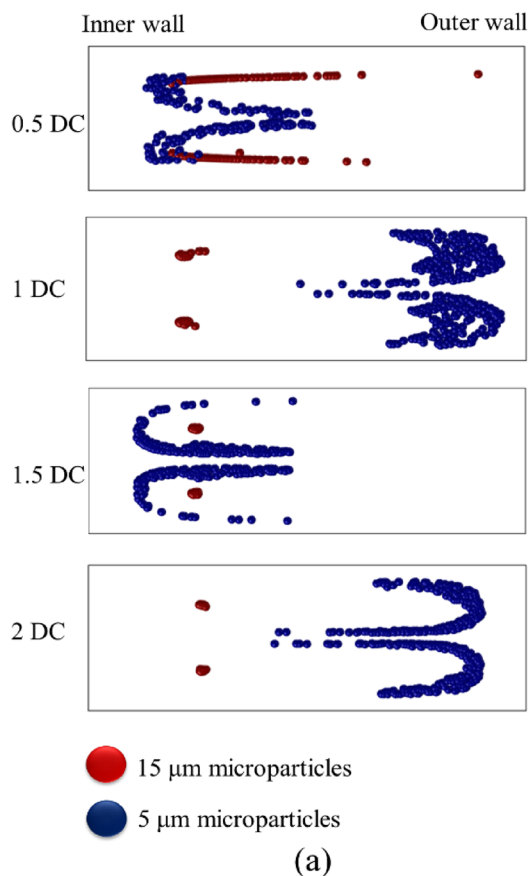


Fig. 3 The simulated cross-sectional position of the 5 and 15 μm polystyrene microparticles at the outlet of the spiral microchannel at various Dean cycles (a). The simulated distance of the 5 and 15 μm

polystyrene microparticles from the inner wall at the outlet as a function of the total flow rate (b). The data in (b) corresponds to the simulation results of (a). The DC indicates the Dean cycle

trajectories based on their sizes. For the larger particles, both forces are relevant. At the central region, the force field resulting from their superposition brings the larger particles to two equilibrium positions. In spite of this fact, all the larger particles should have time to reach the equilibrium positions. As such, there is a lower limit for the total flow rate to inertially focus the larger particles. This fact is apparent in the focusing pattern of the larger particles, shown in Fig. 3b. The focusing position of the larger particles changes with increasing the total flow rate.

The dynamics of the smaller particles are, however, modulated by the Dean drag forces rather than the lift forces. In this extreme, the smaller particles follow two symmetrical vortices, remaining randomly distributed. Since the fluid circulates laterally due to the vortices, the smaller particles are in a continuous lateral circulation. Thus, the positions of the smaller particles at the outlet rely on the geometry of the microfluidic device and the flow rate. The positions are solely subject to the flow rate for a spiral microfluidic device with specified geometry. The positions of the smaller particles oscillate as a function of the flow rate (see Fig. 3). This fact modulates the separation purity for the larger particles. The total flow rate must be at specific values to ensure an integer number of, so-called, Dean cycle to afford the highest separation purity (see Fig. 3).

Considering the aforementioned two constraints for the proper flow rate, we opted the total flow rate of $650 \mu\text{L min}^{-1}$ to ensure both complete inertial migration and 1 Dean cycle. It must be noted that the total flow rate of $1300 \mu\text{L min}^{-1}$, also, satisfies the aforementioned constraints, but we selected $650 \mu\text{L min}^{-1}$ as the opted total flow rate. As PDMS deforms with increasing the flow rate, leading to unreliable results owing to changing the dimensions and shape of the microfluidic device cross section (Jeon et al. 2022).

After selecting the proper flow rates, the separation of the 5 and 15 μm polystyrene microparticles using the spiral microfluidic device was simulated, and compared with the experimental results. The separation results from the simulation and experiments are shown in Fig. 4a–c. It was experimentally obtained that the polystyrene microparticles were separated with the efficiency and purity of 78% and 96.1%, respectively. This finding indicates that the opted flow rates were proper such that the larger particles migrate inertially toward the inner wall while the smaller particles circulate laterally toward the outer wall. Furthermore, our computational results not only confirm this phenomenon but also demonstrate that inertial migration occurs in two stages (see Fig. 4d). In the first stage, particles migrate to two lines where wall-induced and shear-gradient lift forces cancel out each other. In the next step, they slowly move toward the center of the faces due to rotation-induced lift force (Zhou and Papautsky 2013).

6.2 Dynamics of microparticles in the spiral-DEP microfluidic device

Figure 5 demonstrates the contributing forces on the dynamics of the 15 μm polystyrene microparticles in the spiral-DEP microfluidic device. The equilibrium positions of the microparticles are calculated using the constraint $F_{\text{total}} = \mathbf{0}$. It is observed that the equilibrium positions of the 15 μm polystyrene microparticles are modulated in the presence of the DEP force. The real part of the Clausius–Mossotti factor determines the direction of the DEP force. In this context, the real part of the Clausius–Mossotti factor is negative for the 15 μm particles at the frequency of 1 MHz, and the DEP force is directed away from the microelectrodes.

In addition, while the equilibrium position corresponding to the lower wall is considerably displaced, the top wall-associated equilibrium position remains almost intact by the DEP force generated by the microelectrodes. The reason is the short-range nature of the DEP force, which exponentially decays by the distance from the microelectrodes (Sorour Amini and Mohammadi 2023).

We simulated the dynamics of the 15 μm polystyrene microparticles in the presence of the DEP force. In the spiral-DEP microfluidic device, there are no allocated microelectrodes within the initial 1 cm of the spiral microchannel; as such, the lateral position of the microparticles does not change by increasing the voltage within the initial 1 cm. Also, the curvature is less in the initial first turn of the spiral microchannel; thus, the effect of the Dean drag force is significant and the position of the microparticles does not change with varying the voltage in the first 3 cm of the spiral microchannel (region #1 in Fig. 6). In the subsequent region, the 15 μm polystyrene microparticles are gradually directed away from the microelectrodes in the presence of the DEP force (region #2 in Fig. 6). It is observed that a negative DEP force directs the microparticles away from inertial equilibrium positions in the vicinity of the microelectrodes. In this venue, the effect of the DEP force was experimentally examined on the dynamics of the 15 μm polystyrene microparticles. To this end, a sample of the 15 μm polystyrene microparticles was injected into the spiral-DEP microfluidic device at a total flow rate of $650 \mu\text{L min}^{-1}$. Meanwhile, the frequency of the applied electric field was set to 1 MHz and the voltage increased from 0 to 50 V.

Figure 7 depicts the size distribution of the microparticles at the inlet and outlets of the spiral-DEP microfluidic device. The majority of the microparticles ($\sim 96\%$) migrated toward the inner wall in the absence of the DEP force, whereas the microparticles start to migrate toward the outer wall with increasing the voltage as a result of the negative DEP force generated by the microelectrodes (Fig. 7b and c). This indicates that the microelectrodes enable repelling non-target micro- and bioparticles.

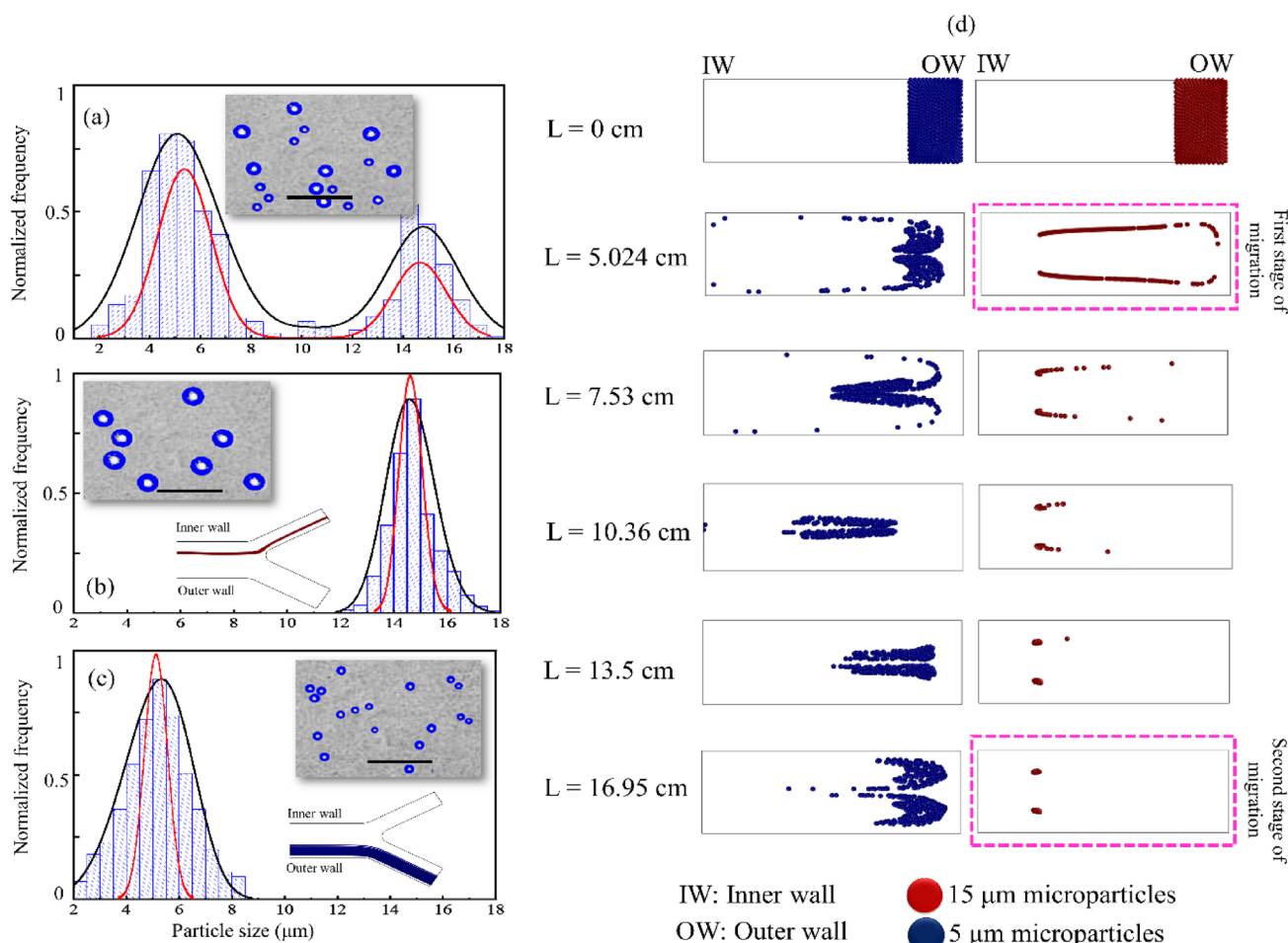


Fig. 4 Size distribution of polystyrene microparticles at the inlet (a), inner outlet (b), and outer outlet (c) of the microfluidic device at the total flow rate of $650 \mu\text{L min}^{-1}$, obtained from the simulation (red lines) and experiments (black lines). Also, the 5 and 15 μm polystyrene microparticles at various cross sections of the spiral micro-

channel (d), ascertained from the simulation. The injected mixture to the spiral microfluidic device comprised 5 and 15 μm polystyrene microparticles in both the simulation and experiments. The scale bars indicate 60 μm . The size distribution in (a–c) was ascertained by the ImageJ software

However, given movie S1 as well as Fig. 7b and c, the microparticles did not completely leave through the outer wall as the equilibrium position corresponding to the top wall remains almost intact by the DEP force generated from the microelectrodes (see Figure S6).

Furthermore, the effect of the DEP force on the dynamics of the 5 μm polystyrene microparticles was computationally and experimentally investigated (see Fig. 8). It is observed that the DEP force does not disrupt the Dean cycle and the 5 μm particles migrate to the outer wall (1 Dean cycle) at the total flow rate of $650 \mu\text{L min}^{-1}$.

To understand the physics underlying this observation, recall the scaling of $|\mathbf{F}_{\text{DEP}}/\mathbf{F}_{\text{Dean}}| \sim d_p^3$ (see equations S4 and 1). Accordingly, the dynamics of the 5 μm particles is modulated by the Dean drag force rather than the DEP force. This indicates that the 5 μm particles are driven by

the Dean vortices. Note, however, that the position of the 5 μm microparticles slightly changes with increasing the voltage (see Fig. 8a). The position of the 5 μm polystyrene microparticles does not notably change until the second turn (region #1), but they, in the third turn, start to migrate toward the outer wall with increasing the voltage (region #2). This fact is associated with the gradual increase of the curvature radius in the spiral microchannel, where the magnitude of the Dean drag force in the third turn is not as strong as that in the first and second turns. Thus, the 5 μm microparticles were slightly pushed toward the outer wall owing to the negative DEP force generated by the microelectrodes. This phenomenon results in the decrement of the width for the microparticle stream at the outlet, which improves the separation purity (see Fig. 8c and d).

Fig. 5 The forces at the cross section of the spiral-DEP microfluidic device for 15 μm polystyrene microparticles at the total flow rate of $650 \mu\text{L min}^{-1}$, voltage of 10 V, and the frequency of 1 MHz. The black-colored arrows indicate the forces. The red-colored dashed circles indicate the equilibrium positions for the 15 μm polystyrene microparticles afforded using the fact that at equilibrium positions $F_{\text{total}} = 0$

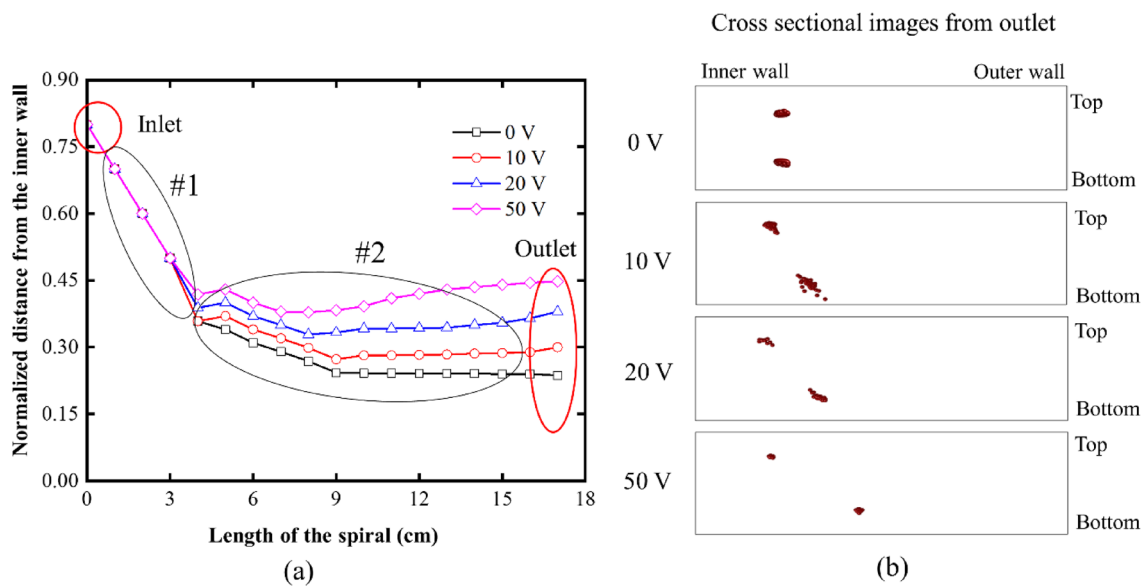
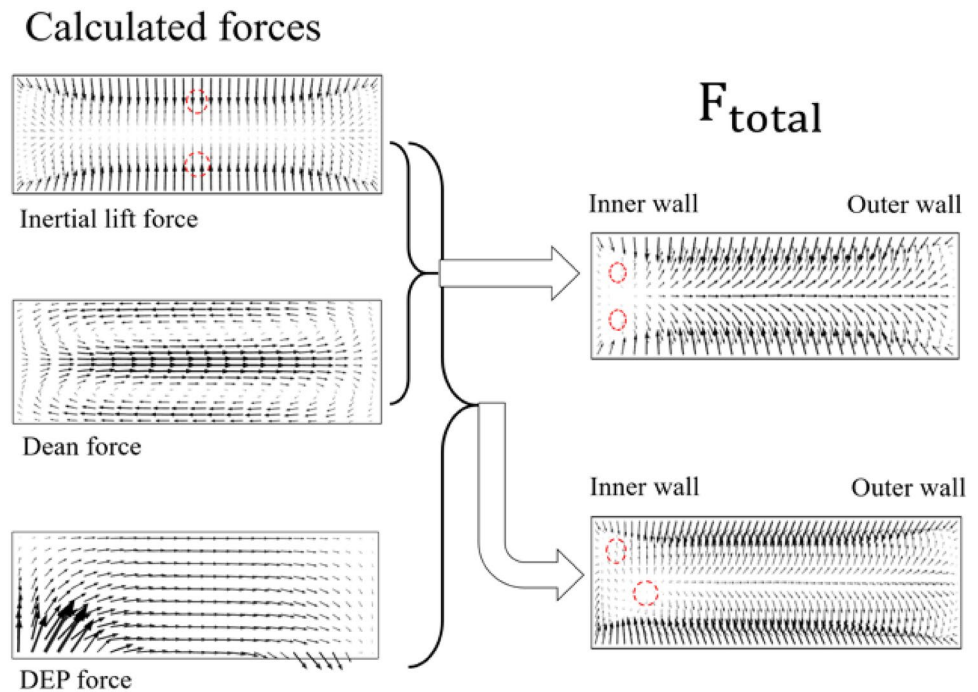


Fig. 6 Simulated distance of the 15 μm polystyrene microparticle from the inner wall at various voltages as a function of the length in the spiral-DEP microfluidic device (a). Simulated cross-sectional

position of the 15 μm polystyrene microparticle at the outlet of the spiral-DEP microfluidic device (b)

6.3 Spiral-DEP microfluidic device in the context of CTCs isolation

A diluted blood sample was injected into the spiral microfluidic device to reject the blood cells through the outer outlet. Figure 9a shows the measured rejection ratio for the diluted blood samples at two distinct hematocrit levels

of 1 and 10% as a function of the total flow rate. The highest rejection ratio was recorded at the total flow rate of $\sim 650 \mu\text{L min}^{-1}$ for the considered hematocrit levels. As also revealed by the plots in the figure, the rejection ratio decreases with increasing the hematocrit level. Needless to say, separating the blood cells from the serum is more difficult at higher hematocrits. The experimental finding in

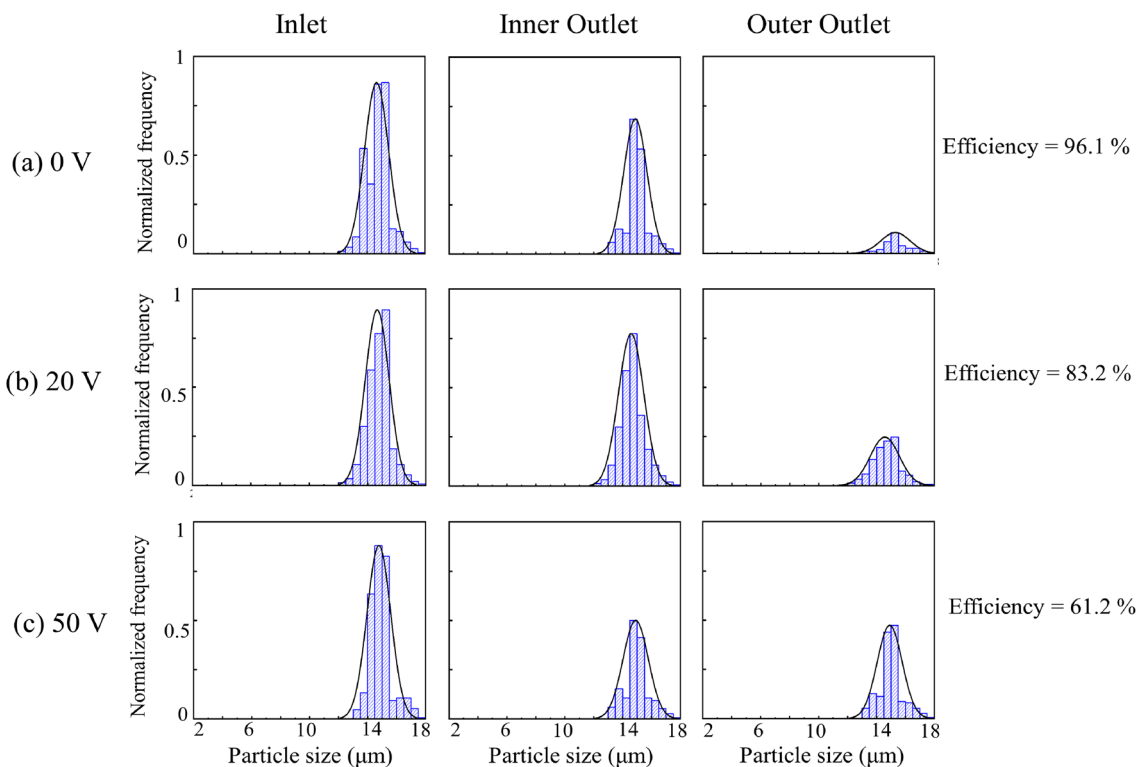


Fig. 7 Experimentally measured size distribution of the 15 μm polystyrene microparticles at the inlet, inner outlet, and outer outlet of the spiral-DEP microfluidic device at the total flow rate of $650 \mu\text{L min}^{-1}$ as a function of the applied voltage

Fig. 9a is partly interpreted through investigating Fig. 9b. Figure 9b illustrates microscale pictures from the distribution of the blood cells at two distinct hematocrit levels of 1 and 10% within the spiral microchannel furnished from the experimental trial. The figure indicates the broadening of the band for the blood cells at the increased hematocrit level.

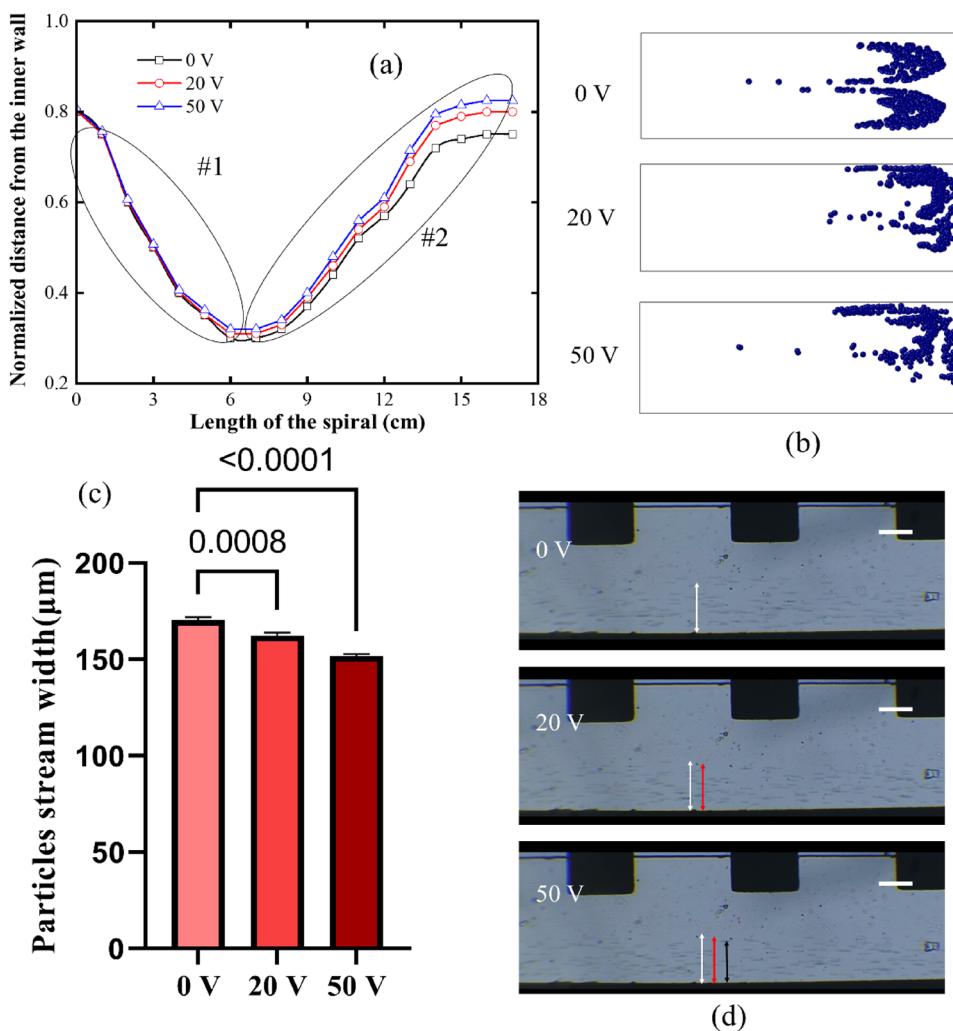
In the next step, a diluted blood sample at the hematocrit level of 1% was spiked with the MDA-MB-231 cell line and injected into the spiral-DEP microfluidic device to separate the CTCs. For this purpose, the total flow rate was fixed at $650 \mu\text{L min}^{-1}$ in which the higher rejection ratio for blood cells was achieved. The frequency was also set to 30 kHz. At this frequency, the Clausius–Mossotti factor for the MDA-MB-231 cell line is close to zero while the factor is negative for all the other blood cells (see Fig. 2b). The influence of the voltage on the separation purity is presented in Fig. 9d. At zero voltage, the obtained cell composition at the inner outlet was 1.6, 13.1, and 85.3% for, respectively, RBCs, WBCs, and MDA-MB-231 cells. This furnishes the purity of 85.3% for the isolated CTCs at zero voltage. At the voltage of 50 V, the obtained cell composition at the inner outlet was 0.5, 5.4, and 94.1% for, respectively, RBCs, WBCs, and MDA-MB-231 cells. This affords the purity of 94.1% for the isolated CTCs at zero voltage.

The purity, however, shows an ascending trend by increasing the voltage. This observation is associated with the forces contributing to the cell dynamics in the spiral-DEP microfluidic device, which are the inertial lift, Dean drag, and DEP forces. At zero voltage, the CTCs were isolated under the influence of hydrodynamic forces that distinguish cells based on their sizes. With increasing the voltage, the DEP force modulates the dynamics of the bioparticles. The negative DEP force generated by the microelectrodes contributes to removing large WBCs that the spiral microfluidic device could not remove.

We also performed flow cytometry experiments on the inner outlet from the spiral-DEP microfluidic device in the absence and presence of the DEP. The histograms from the experiments are shown in Fig. 9h. It is observed that the CD45 expression on WBCs was reduced when the voltage increased from 0 to 50 V. Decreasing the CD45 expression indicates that the negative DEP force generated by the microelectrodes repelled large WBCs away from the inner wall, resulting in higher purity for the isolated CTCs.

Let us continue with the task of addressing the impact of the DEP force on the separation efficiency of the CTCs. While the efficiency was found 88.0% in the absence of DEP, the efficiency was 89.0% for the total flow rate of $650 \mu\text{L min}^{-1}$ and the applied voltage of 50 V. Therefore, the

Fig. 8 Simulated distance of the 5 μm polystyrene microparticles from the inner wall at various voltages as a function of the length in the spiral-DEP microfluidic device (a). Simulated lateral position of the 5 μm polystyrene microparticles at the outlet of the spiral-DEP microfluidic device at various voltages (b). Particle stream width at different voltages ascertained by image processing using the ImageJ software (c). Microscopic images from the 5 μm polystyrene particles in the outer region of the spiral-DEP microfluidic device at 0, 20, and 50 V (d). The scale bars indicate 100 μm



DEP does not have a considerable effect on the efficiency. This fact arises from the selected frequency at which the CTCs experience a relatively small DEP force.

Finally, the effect of the cell separation by the spiral-DEP microfluidic device on the viability of the isolated CTCs was explored. During the operation, the cells experience stresses from two distinct forces: hydrodynamic (lift and Dean drag) and DEP forces. Moreover, the applied electric fields may generate joule heating, elevating the temperature of the medium, which, in turn, may jeopardize the viability of the cells (Cha et al. 2021). Nevertheless, Fig. 9e indicates that the viability was not considerably changed in the operations undertaken in this study.

7 Conclusion

In this study, an inertial-DEP platform with laterally allocated microelectrodes was introduced for the label-free isolation of CTCs from diluted blood samples. To this end, the

particle dynamics were first examined in the presence of inertial lift, Dean drag, and DEP forces by the computational fluid dynamics simulations. In this regard, a direct numerical simulation was conducted to scrutinize the dynamics. Next, the designed inertial-DEP platform was fabricated using standard soft- and photolithography procedures. Then, the performance of the fabricated microfluidic device was tested in solely-inertial and inertial-DEP modes using non-biological and biological samples. As a proof-of-concept, we thoroughly examined the effect of DEP on 5 and 15 μm polystyrene microparticles. It was shown that large non-target micro- and bioparticles can be removed without disrupting the Dean cycle with the aid of negative DEP force generated by the microelectrodes. Finally, diluted blood samples spiked with MDA-MB-231 (2×10^4 CTCs mL⁻¹) cell line were injected into the platform for the separation of MDA-MB-231 cells. Using the proposed spiral-DEP microfluidic device, the MDA-MB-231 cells were captured with 89% efficiency at the total flow rate of 650 μL min⁻¹ without notable changes in viability. While the purity of the isolated CTCs

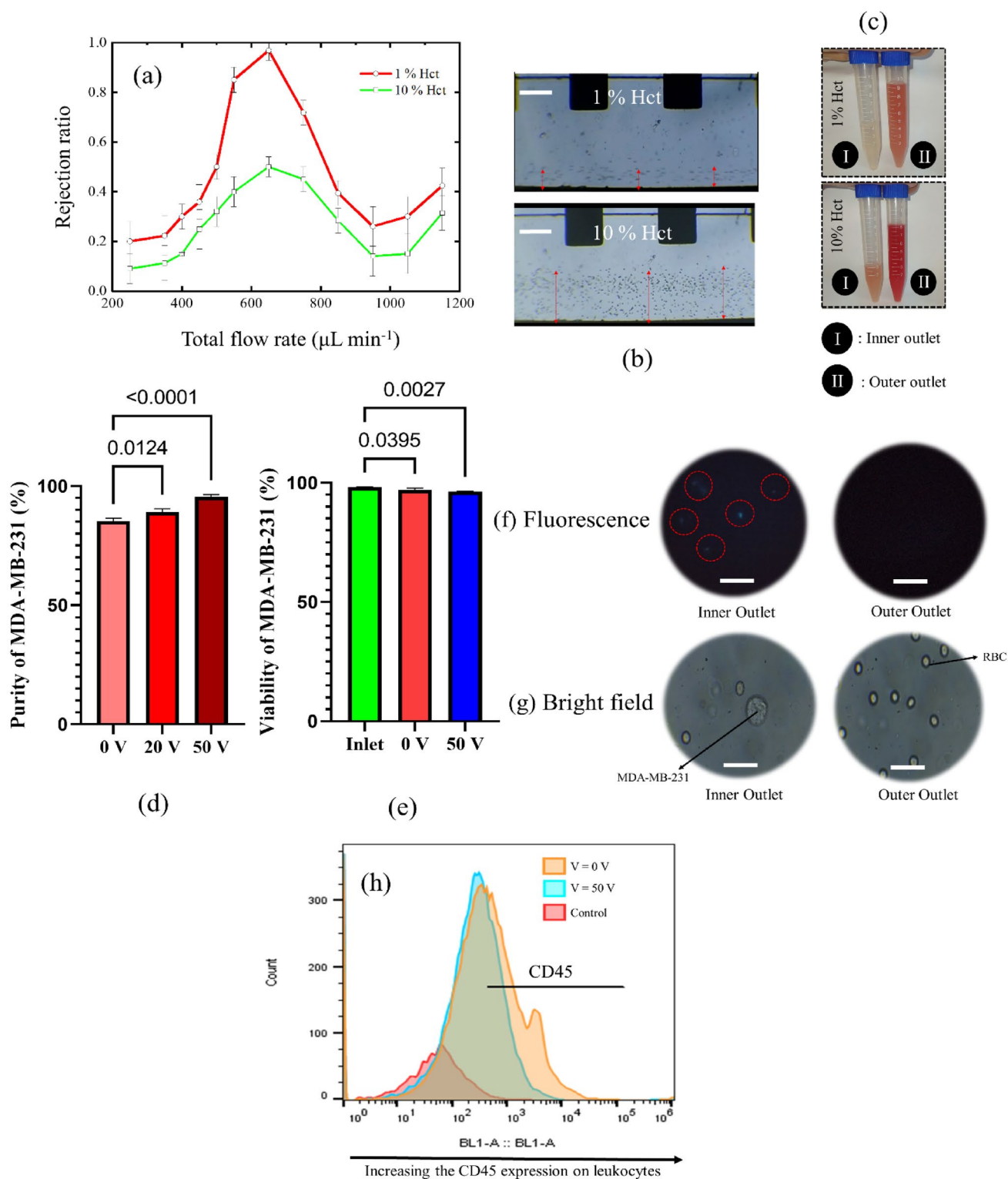


Fig. 9 The rejection ratio as a function of the total flow rate for the diluted blood samples (a). The influence of the blood Hct on the stream width of the blood cells at the outlet from the spiral microfluidic device (b). The collected samples from the inner and outer outlets of the spiral microfluidic device for the sample and sheath flow rates of, respectively, 100 and 550 $\mu\text{L min}^{-1}$ (c). The effect of the voltage on the separation purity (d). The viability of the MDA-MB-231 cells before and after injection to the spiral-DEP microflu-

idic device (e). Fluorescence images from the inner and outer outlets in which the blue-colored dots are MDA-MB-231 cells, stained with DAPI (f). Bright-field images from the inner and outer outlets (g). CD45 expression on leukocytes in the absence and presence of DEP (h). The scale bars indicate 139, 25, and 25 μm in, respectively, (b), (f), and (g). The plots in (a), (d), and (e) represent the mean value and the standard deviation ($n = 3$ and p value = 0.05)

was 85.3% in the absence of the DEP, the purity increased to 94.1% under the voltage of 50 V.

Supplementary Information The online version contains supplementary material available at <https://doi.org/10.1007/s10404-023-02662-3>.

Acknowledgements The authors would like to thank the sharif university of technology research council for the support.

Author contributions AM supervised the project. MS and AM wrote the main manuscript text along with simulation, fabrication, and testing of the microfluidic device. MR prepared biological samples along with editing the manuscript.

Data availability There is no data availability to declare.

Declarations

Conflict of interest The authors state that there is no conflict of interest.

References

- Aghaamoo M, Aghilinejad A, Chen X, Xu J (2019) On the design of deterministic dielectrophoresis for continuous separation of circulating tumor cells from peripheral blood cells. *Electrophoresis* 40(10):1486–1493
- Au SH, Edd J, Stoddard AE, Wong KH, Fachin F, Maheswaran S, Haber DA, Stott SL, Kapur R, Toner M (2017) Microfluidic isolation of circulating tumor cell clusters by size and asymmetry. *Sci Rep* 7(1):1–10
- Bazaz SR, Mihandust A, Salomon R, Joushani HAN, Li W, Amiri HA, Mirakhorli F, Zhand S, Shrestha J, Miansari M (2022) Zig-zag microchannel for rigid inertial separation and enrichment (Z-RISE) of cells and particles. *Lab Chip* 22(21):4093–4109
- Buican TN, Smyth MJ, Crissman HA, Salzman GC, Stewart CC, Martin JC (1987) Automated single-cell manipulation and sorting by light trapping. *Appl Opt* 26(24):5311–5316
- Cha H, Fallahi H, Dai Y, Yuan D, An H, Nguyen N-T, Zhang J (2021) Multiphysics microfluidics for cell manipulation and separation: a review. *Lab Chip* 22(3):423–444. <https://doi.org/10.1039/D1LC00869B>
- Di Carlo D (2009) Inertial microfluidics. *Lab Chip* 9(21):3038–3046
- Di Carlo D, Edd JF, Humphry KJ, Stone HA, Toner M (2009) Particle segregation and dynamics in confined flows. *Phys Rev Lett* 102(9):094503
- Erdem K, Ahmadi VE, Kosar A, Kuddusi L (2020) Differential sorting of microparticles using spiral microchannels with elliptic configurations. *Micromachines* 11(4):412
- Esmailsabzali H, Beischlag TV, Cox ME, Parameswaran AM, Park EJ (2013) Detection and isolation of circulating tumor cells: principles and methods. *Biotechnol Adv* 31(7):1063–1084
- Fallahi H, Zhang J, Phan H-P, Nguyen N-T (2019) Flexible microfluidics: fundamentals, recent developments, and applications. *Micromachines* 10(12):830
- Fetah KL, DiPardo BJ, Kongadzem EM, Tomlinson JS, Elzagheid A, Elmusrati M, Khademhosseini A, Ashammakhi N (2019) Cancer modeling-on-a-chip with future artificial intelligence integration. *Small* 15(50):1901985
- Gertler R, Rosenberg R, Fuehrer K, Dahm M, Nekarda H, Siewert JR (2003) Detection of circulating tumor cells in blood using an optimized density gradient centrifugation, molecular staging of cancer. Springer, pp 149–155
- Ghadami S, Kowsari-Esfahan R, Saidi MS, Firoozbakhsh K (2017) Spiral microchannel with stair-like cross section for size-based particle separation. *Microfluid Nanofluid* 21(7):1–10
- Gijzen FJ, van de Vosse FN, Janssen J (1999) The influence of the non-Newtonian properties of blood on the flow in large arteries: steady flow in a carotid bifurcation model. *J Biomech* 32(6):601–608
- Goh KY, Lim W-T (2018) Profiling circulating tumour cells for clinical applications. *Liquid biopsy*. IntechOpen
- Guan X (2015) Cancer metastases: challenges and opportunities. *Acta Pharmaceutica Sinica B* 5(5):402–418
- Guan G, Wu L, Bhagat AA, Li Z, Chen PC, Chao S, Ong CJ, Han J (2013) Spiral microchannel with rectangular and trapezoidal cross-sections for size based particle separation. *Sci Rep* 3(1):1–9
- Habli Z, AlChamaa W, Saab R, Kadara H, Khraiche ML (2020) Circulating tumor cell detection technologies and clinical utility: challenges and opportunities. *Cancers* 12(7):1930
- Hao S-J, Wan Y, Xia Y-Q, Zou X, Zheng S-Y (2018) Size-based separation methods of circulating tumor cells. *Adv Drug Deliv Rev* 125:3–20
- Ho B, Leal L (1974) Inertial migration of rigid spheres in two-dimensional unidirectional flows. *J Fluid Mech* 65(2):365–400
- Hou HW, Warkiani ME, Khoo BL, Li ZR, Soo RA, Tan DS-W, Lim W-T, Han J, Bhagat AAS, Lim CT (2013) Isolation and retrieval of circulating tumor cells using centrifugal forces. *Sci Rep* 3(1):1–8
- Huang D, Xiang N (2021) Rapid and precise tumor cell separation using the combination of size-dependent inertial and size-independent magnetic methods. *Lab Chip* 21(7):1409–1417
- Jeon H, Kwon T, Yoon J, Han J (2022) Engineering a deformation-free plastic spiral inertial microfluidic system for CHO cell clarification in biomanufacturing. *Lab Chip* 22(2):272–285
- Khan M, Chen X (2022) Numerical study of dielectrophoresis-modified inertial migration for overlapping sized cell separation. *Electrophoresis* 43(7–8):879–891
- Kim U, Oh B, Ahn J, Lee S, Cho Y (2022) Inertia-acoustophoresis hybrid microfluidic device for rapid and efficient cell separation. *Sensors* 22(13):4709
- Lee MG, Shin JH, Bae CY, Choi S, Park J-K (2013) Label-free cancer cell separation from human whole blood using inertial microfluidics at low shear stress. *Anal Chem* 85(13):6213–6218
- Lim H, Back SM, Hwang MH, Lee D-H, Choi H, Nam J (2019) Sheathless high-throughput circulating tumor cell separation using viscoelastic non-Newtonian fluid. *Micromachines* 10(7):462
- Liu Y, Zhao W, Cheng R, Hodgson J, Egan M, Pope CNC, Nikolidakos PG, Mao L (2021) Simultaneous biochemical and functional phenotyping of single circulating tumor cells using ultrahigh throughput and recovery microfluidic devices. *Lab Chip* 21(18):3583–3597
- Mach AJ, Kim JH, Arshi A, Hur SC, Di Carlo D (2011) Automated cellular sample preparation using a centrifuge-on-a-chip. *Lab Chip* 11(17):2827–2834
- Mishra A, Dubash TD, Edd JF, Jewett MK, Garre SG, Karabacak NM, Rabe DC, Mutlu BR, Walsh JR, Kapur R (2020) Ultrahigh-throughput magnetic sorting of large blood volumes for epitope-agnostic isolation of circulating tumor cells. *Proc Natl Acad Sci* 117(29):16839–16847
- Mohammadi A (2015) Transport in droplet-hydrogel composites: response to external stimuli. *Colloid Polym Sci* 293(3):941–962
- Ozkumur E, Shah AM, Ciciliano JC, Emmink BL, Miyamoto DT, Brachtel E, Yu M, Chen P-I, Morgan B, Trautwein J (2013) Inertial focusing for tumor antigen-dependent and-independent sorting of rare circulating tumor cells. *Sci Transl Med* 5(179):179ra47–179ra47
- Pødenphant M, Ashley N, Koprowska K, Mir KU, Zalkovskij M, Bilenbergh B, Bodmer W, Kristensen A, Marie R (2015) Separation of

- cancer cells from white blood cells by pinched flow fractionation. *Lab Chip* 15(24):4598–4606
- Rahmani A, Mohammadi A, Kalhor HR (2018) A continuous flow microfluidic device based on contactless dielectrophoresis for bioparticles enrichment. *Electrophoresis* 39(3):445–455
- Sharma S, Zhuang R, Long M, Pavlovic M, Kang Y, Ilyas A, Asghar W (2018) Circulating tumor cell isolation, culture, and downstream molecular analysis. *Biotechnol Adv* 36(4):1063–1078
- Shrestha J, Bazaz SR, Ding L, Vasilescu S, Idrees S, Söderström B, Hansbro PM, Ghadiri M, Warkiani ME (2023) Rapid separation of bacteria from primary nasal samples using inertial microfluidics. *Lab Chip* 23(1):146–156
- Siegel R, Miller KD, Jemal A (2014) Cancer statistics, 2012. *CA Cancer J Clin* 64(1):9–29
- Sleeboom JJ, Eslami Amirabadi H, Nair P, Sahlgren CM, Den Toonder JM (2018) Metastasis in context: modeling the tumor microenvironment with cancer-on-a-chip approaches. *Dis Model Mech* 11(3):dmm033100
- Sorour Amini H, Mohammadi A (2023) Microparticle separation using dielectrophoresis-assisted inertial microfluidics: a GPU-accelerated immersed boundary-lattice Boltzmann simulation. *Phys Rev E* 107(3):035307
- Sun J, Li M, Liu C, Zhang Y, Liu D, Liu W, Hu G, Jiang X (2012) Double spiral microchannel for label-free tumor cell separation and enrichment. *Lab Chip* 12(20):3952–3960
- Undvall Anand E, Magnusson C, Lenshof A, Ceder Y, Lilja H, Laurell T (2021) Two-step acoustophoresis separation of live tumor cells from whole blood. *Anal Chem* 93(51):17076–17085
- Wang L, Lu J, Marchenko SA, Monuki ES, Flanagan LA, Lee AP (2009) Dual frequency dielectrophoresis with interdigitated sidewall electrodes for microfluidic flow-through separation of beads and cells. *Electrophoresis* 30(5):782–791
- Warkiani ME, Guan G, Luan KB, Lee WC, Bhagat AAS, Chaudhuri PK, Tan DS-W, Lim WT, Lee SC, Chen PC (2014) Slanted spiral microfluidics for the ultra-fast, label-free isolation of circulating tumor cells. *Lab Chip* 14(1):128–137
- Xiang N, Ni Z (2022) Inertial microfluidics: current status, challenges, and future opportunities. *Lab Chip* 22(24):4792–4804. <https://doi.org/10.1039/D2LC00722C>
- Yafouz B, Kadri NA, Ibrahim F (2014) Dielectrophoretic manipulation and separation of microparticles using microarray dot electrodes. *Sensors* 14(4):6356–6369
- Yang C, Xia B-R, Jin W-L, Lou G (2019) Circulating tumor cells in precision oncology: clinical applications in liquid biopsy and 3D organoid model. *Cancer Cell Int* 19(1):1–13
- Zhang J, Yan S, Sluyter R, Li W, Alici G, Nguyen N-T (2014) Inertial particle separation by differential equilibrium positions in a symmetrical serpentine micro-channel. *Sci Rep* 4(1):1–9
- Zhang J, Yuan D, Zhao Q, Yan S, Tang S-Y, Tan SH, Guo J, Xia H, Nguyen N-T, Li W (2018) Tunable particle separation in a hybrid dielectrophoresis (DEP)-inertial microfluidic device. *Sens Actuators B Chem* 267:14–25
- Zhang H, Chang H, Neuzil P (2019) DEP-on-a-chip: Dielectrophoresis applied to microfluidic platforms. *Micromachines* 10(6):423
- Zhao W, Zhu T, Cheng R, Liu Y, He J, Qiu H, Wang L, Nagy T, Querec TD, Unger ER (2016) Label-free and continuous-flow ferrohydrodynamic separation of HeLa cells and blood cells in biocompatible ferrofluids. *Adv Func Mater* 26(22):3990–3998
- Zheng S, Lin H, Liu J-Q, Balic M, Datar R, Cote RJ, Tai Y-C (2007) Membrane microfilter device for selective capture, electrolysis and genomic analysis of human circulating tumor cells. *J Chromatogr A* 1162(2):154–161
- Zhou J, Papautsky I (2013) Fundamentals of inertial focusing in microchannels. *Lab Chip* 13(6):1121–1132
- Zhu S, Jiang F, Han Y, Xiang N, Ni Z (2020) Microfluidics for label-free sorting of rare circulating tumor cells. *Analyst* 145(22):7103–7124

Publisher's Note Springer Nature remains neutral with regard to jurisdictional claims in published maps and institutional affiliations.

Springer Nature or its licensor (e.g. a society or other partner) holds exclusive rights to this article under a publishing agreement with the author(s) or other rightsholder(s); author self-archiving of the accepted manuscript version of this article is solely governed by the terms of such publishing agreement and applicable law.